

NT's HC \$3.75

THE BEHAVIOR OF PARALLEL AIR JETS

J. G. Edler v. Bohl

(NASA-TT-F-14653) THE BEHAVIOR OF
PARALLEL AIR JETS (Scientific Translation
Service) 34 p HC \$3.75

N73-15311

Unclas
G3/12 52622

Translation of: "Das Verhalten
paralleler Luftstrahlen," Ingenieur-
Archiv, Vol. 11, 1940, pp. 295 - 314.



NATIONAL AERONAUTICS AND SPACE ADMINISTRATION
WASHINGTON, D. C. 20546 JANUARY 1973

1. Report No. NASA TT F-14,653		2. Government Accession No.		3. Recipient's Catalog No.	
4. Title and Subtitle THE BEHAVIOR OF PARALLEL AIR JETS				5. Report Date January 19, 1973	
				6. Performing Organization Code	
7. Author(s) J. G. Edler v. Bohl				8. Performing Organization Report No.	
				10. Work Unit No.	
9. Performing Organization Name and Address SCITRAN Box 5456 Santa Barbara, CA 93108				11. Contract or Grant No. NASw-2483	
				13. Type of Report and Period Covered Translation	
12. Sponsoring Agency Name and Address National Aeronautics and Space Administration Washington, D.C. 20546				14. Sponsoring Agency Code	
15. Supplementary Notes Translation of: "Das Verhalten paralleler Luftstrahlen," Ingenieur-Archiv, Vol. 11, 1940, pp. 295 - 314.					
16. Abstract The flow behind three grids having different opening sizes was studied to explain irregularities in the flow behind smoothing grids. A probe which could be calibrated in a free jet mixing zone was developed. For the grids studied it appears that the instability observed occurs more easily as lattice rods of constant width are placed closer together. This phenomenon was followed up theoretically.					
17. Key Words (Selected by Author(s))				18. Distribution Statement Unclassified - Unlimited	
19. Security Classif. (of this report) Unclassified		20. Security Classif. (of this page) Unclassified		21. No. of Pages 33	22. Price 3.75

THE BEHAVIOR OF PARALLEL AIR JETS

J. G. Edler v. Bohl

ABSTRACT. The flow behind three grids having different opening sizes was studied to explain irregularities in the flow behind smoothing grids. A probe which could be calibrated in a free jet mixing zone was developed. For the grids studied it appears that the instability observed occurs more easily as lattice rods of constant width are placed closer together. This phenomenon was followed up theoretically.

Introduction

/295*

This work ⁽¹⁾ is intended to explain the irregularities which are observed in the flow behind the smoothing grids of blowers and wind tunnels, and which persist there, in that several of the jets produced in the grid join together, working against the smoothing out of the air stream. For simplicity, only the plane flow produced by grids consisting of rods with parallel edges is investigated. It was found, in fact, that under certain conditions every pair of air jets combines. Now, because of its greater wavelength, this irregularity persists in the flow longer than if the jets had remained separate. This undesired phenomenon proves to be dependent on the density of the grid, i. e., on the magnitude of the ratio

$$\lambda = \frac{\text{obstructed area}}{\text{channel cross section}}$$

* Numbers in the margin indicate pagination in the original foreign text.

(1) Göttingen dissertation. Prof. Dr. L. Prandtl, reporter; Prof. Dr. A. Betz, co-reporter.

When λ_1 is small the jets passing through the grid remain parallel to the long axis of the channel, but with large λ_1 they become unstable and attract each other so that they combine. The border between the two cases lies between $\lambda_1 = 0.37$ and $\lambda_1 = 0.46$. This is determined from measurements behind several grids for which λ_1 is increased or decreased by a change in the number of lattice bars. This shows that the flow behind a smoothing grid will become more uneven the more densely it is constructed, as long as a certain limiting value for the density is exceeded. At small densities, of course, the smoothing action which takes place due to the narrowing of cross section, would be small. Therefore, the density must approach the limit for the highest degree of smoothing.

Now, in order to obtain useful velocity measurements in the particularly strong turbulent flow occurring in our grid measurements, it was necessary to find a new probe which would provide a measure of the static pressure in turbulent flow. The usual probe types for smooth flow fail as soon as the flow becomes strongly turbulent, because here the flow direction varies considerably about a central value. The cause of this failure can be found in the great sensitivity to obliquely incident flow. G. Cordes ⁽²⁾ was able to measure the static pressure from measurements with a small disk probe and a "turbulence probe" which was intended to determine the turbulent transverse flows perpendicular to the plane of the disk. He was successful only for weak turbulence. Following a suggestion from Prof. Prandtl, Mustert ⁽³⁾ has used a probe which makes use of the fact that in flow around a cylinder, the position of the point of boundary layer separation depends on the strength of the turbulence. By pressure measurements at three definite points of such a cylinder used as a probe, Mustert was able to determine a measure for the strength of turbulence of a non-laminar flow. In this work, the probe is placed parallel to the edge generating the turbulence. This avoids a perturbing flow in the dead volume in the direction of the

(2) G. Cordes, Ing.-Arch. 8(1937)page 245.

(3) Previously unpublished.

cylinder axis, which would falsify the pressure indications ⁽⁴⁾.

A dimensionless measure of the turbulence is derived from these pressure indications and made dependent upon a similar expression containing the static pressure. In this way a calibration curve was found through measurements in a free jet mixing zone. From this calibration curve, the static pressure can be determined with some reliability in other turbulent flows.

It should be mentioned that the turbulences occurring behind the bar grids used here are considerably stronger than those observed in a free jet mixing zone, so that even total pressure measurements with an ordinary pitot tube are no longer sufficient. The angular range within which the flow direction changes continuously due to turbulence, is far greater than the directional sensitivity of a pitot tube. But fortunately, we were also able to overcome these problems fairly well, as shown below.

I. Experimental Part

1. The Test System

The air flow necessary for the measurements was generated by a two-stage axial blower, a (Figure 1). The air drawn through the propellers is led through a circular tube section, b, and a transition section, c, which changes the circular cross section into a rectangular one, and into a smoothing channel, d, which is 60 cm high and 65 cm wide. The nozzle, e, of the blower decreases the cross section to 32 cm high while the width remains the same. A flow straightener, f, is placed at the entrance of the smoothing section. Following it are three screens, g_1 , g_2 , and g_3 . Likewise, the transition section and the tubular section each contain one

(4) Because of his experimental conditions, Mustert was compelled to place the probe perpendicular to the edge generating the turbulence, so that he had to come to terms with the problem just mentioned.

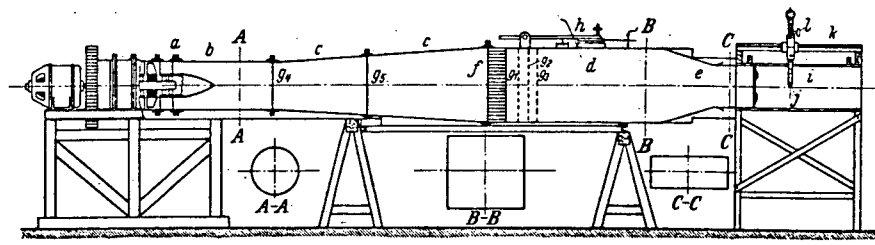


Figure 1. The blower used.

smoothing screen, g_4 and g_5 .

Small pressure fluctuations were compensated by means of a pressure regulator, h , according to Schrenk ⁽⁵⁾, and larger ones by controlling the rate of motor rotation with a shunt resistance.

The test section, i , consisted of a channel 100 cm long, with the same cross section as the nozzle. An opening 82 cm long and 4 cm wide was left in the top so that the probe, j , could be introduced and moved in the flow direction along a prismatic guide, k , and across the flow direction by a rack and pinion drive, l . The remaining openings were closed with suitable pieces of wood.

The lateral boundaries of the test section consisted of double walls, with the inner wall being 12 cm shorter than the outer one, and with the different grids fastened to the ends. The walls were 1.8 cm thick.

The horizontal grid bars consisted of strips 5 cm wide and 1.4 cm thick, with trapezoidal cross section. The wider sides were turned toward the flow. Careful attention was paid to the beveling, in order to get clean separation. The bars were fastened with countersunk bolts and nuts to two vertical strips, and these were

/ 297

(5) O. Schrenk, Ing.-Arch. 1(1930), page 350.

screwed to the ends of the inner channel walls. Behind this, profile strips 6.5 cm wide were placed at both sides, gradually converting the channel width down to the true test section width, which is less by twice the thickness of the inner channel wall, while avoiding a step which would produce a separation.

Figure 1a shows the grid with the smallest λ which was studied (stable case). For all three grids studied, the bars were arranged so that the widths of the jets adjacent to the upper and lower channel walls, measured in the plane of the grid, were $2/3$ the width of a central jet. The reasoning on which this is based follows below. The corresponding values for λ were:

- (I) 0.308
- (II) 0.462
- (III) 0.615

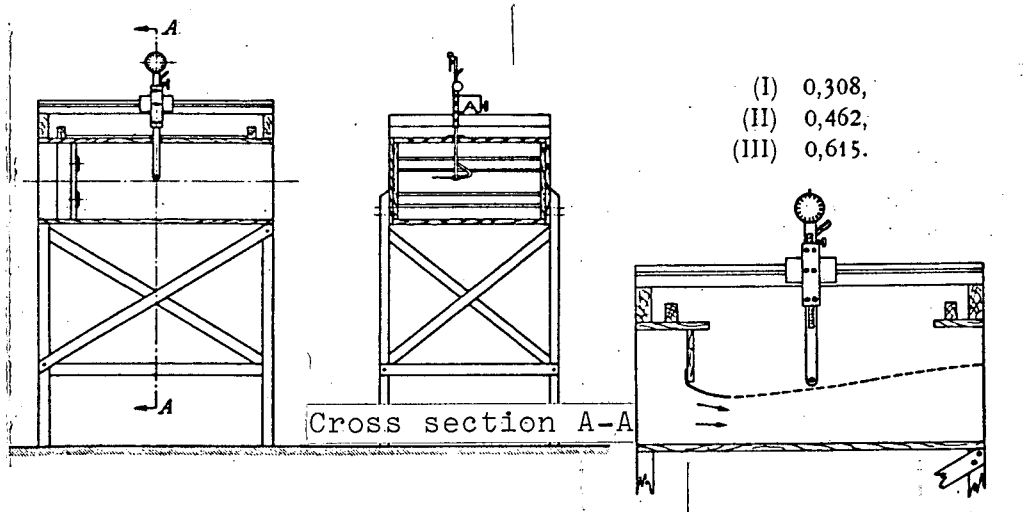


Figure 1a. Test system with grid I inserted.

Figure 1b. Test system for probe calibration.

To calibrate the probe, the top of the channel was removed as far as the nozzle. Instead of the grid, a board with a curved sheet shaped as shown in Figure 1b was inserted, covering the upper half of the channel cross section at a width of 20 cm. The static pressure in the mixing zone of the jet passing through the cross section which is reduced in this manner can, with sufficient accuracy, be taken as

zero. According to Tollmien⁽⁶⁾, the static pressure in the free jet is about $\frac{1}{2}\%$ of the dynamic pressure.

The pressure, compared to the pressure prevailing in the test room, was measured with an alcohol-filled vertical manometer according to Prandtl. It was evaluated with consideration of the temperature and barometer reading.

2. The Probes Used and the Measuring Process

A small tube of circular cross section and 2 mm diameter, with a hole 0.2 mm in diameter was used as a probe to determine the static pressure and the total pressure (j in Figure 2). The hole was 6 mm from the closed end of the tube. Flow was incident on the tube perpendicular to its long axis. For the position just mentioned, the deviation of the stream lines in the direction of this axis had no effect on the pressure indications, as was shown by comparison with a probe having its hole in the middle. It was held parallel to the grid bars by a streamlined support, m. At its upper end is a disk, n, graduated in degrees, which, by means of a thin steel cable, o, connecting the two pulleys, provides for rotation of the probe by about 360°. The pulley at the lower end of the support, p, is designed so that the probe can be changed. The pressure is carried from the probe through a short hose section, r, into a brass tube, q, carried by the support.

/ 298

Now the pressure readings from the probe were recorded as a function of the angle of rotation for various degrees of turbulence in the free jet mixing zone. Let the maximum pressure be designated as a. As we shall see later, this is equal to the total pressure only for very low turbulence. The minimum, which lies at 70° (because of the symmetry of the pressure distribution, it makes no difference which way the probe is rotated) can be called b. On further rotation, we detect the separation of the boundary layer

(6) W. Tollmien, Z. angew. Math. Mech. 6(1926), page 468.

by the subsequent pressure increase. The pressure at 115° is called c. The curves of Figure 3 have been recorded at locations of different strengths of turbulence behind grid I ($\alpha = 0.308$). Here, it can clearly

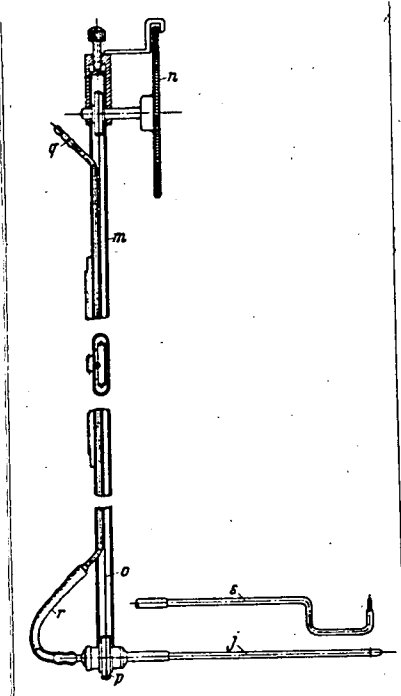


Figure 2. The two probes.

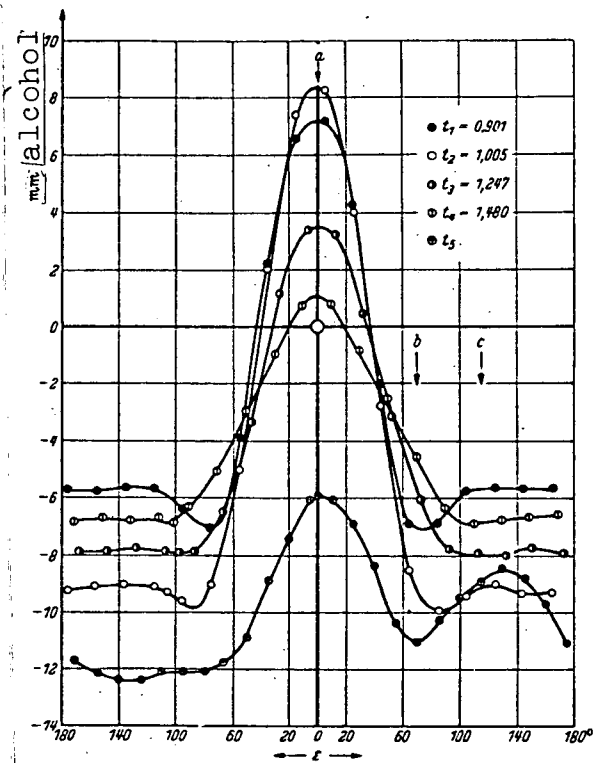


Figure 3. Pressure readings from the probe as a function of the angle of rotation for different strengths of turbulence.

be seen how the separation occurs later and later with increasing turbulence (curves t_1 to t_4). The pressure increase becomes steadily weaker. When t becomes larger than 1.5, we enter a region in which the eddies from the upper and lower edges of a grid bar strike the probe, one from above and one from below, as a concentrated pattern of eddies, so that curve t_5 in Figure 3 shows two stagnation points at 0° and 130° . In this region, then, no useful results could be obtained. As a measure of turbulence, we have selected

the expression used by Mustert:

$$t = \frac{a - c}{a - b}$$

In order to obtain a calibration curve for our probe to determine the static pressure, we, like Mustert, plotted the ratio $(a - p_{st})/(a - b)$ versus t as the abscissa. Here a , b , and c were obtained by measurements in the free jet (See Figure 4).

/ 299

In order to determine whether the calibration curve obtained in this manner is independent of the dynamic pressure and the Reynolds number, measurements were made in the free jet mixing zone at four different velocities. The velocities at the center of the jet were

27.5 m/s 20.3 m/s 13.6 m/s 10.2 m/s

The pressure, a , at a distance of 49 cm from the edge of the nozzle is plotted in Figure 5 in mm alcohol. Measurements were also made at the same velocities at distances of 26 cm, 36 cm, and 60 cm from the nozzle edge. At low values of a the calibration points scattered so severely that the calibration curve could not be determined past $t = 1.00$.

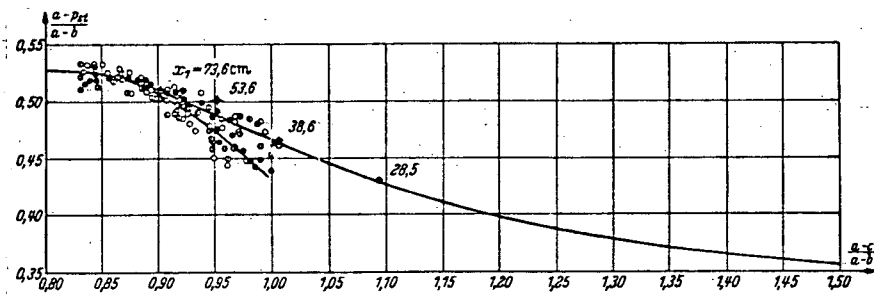


Figure 4. Calibration curve for calculation of the static pressure.

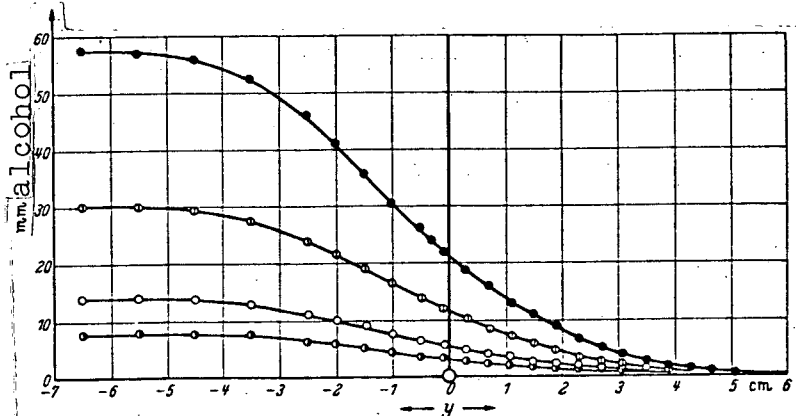


Figure 5. Pressure distribution in the free jet.

In measurements behind the bar grids, two problems which at first seemed insuperable were met: It appeared that the turbulence produced by our grids was considerably stronger than that which was observed in a free jet mixing zone, so that our calibration curve would be good only for measurements at very great distance from the grid. The second problem was in the determination of the total pressure. A pitot tube, s , was attached to the support in such a way that its opening was at the same position as the hole in our probe (see Figure 2). In a flow for which the turbulence was not greater than that in the mixing zone of a free jet, the pitot tube indicated the total pressure with sufficient accuracy. But if we enter a more strongly turbulent flow, the flow direction varies through a greater angle than the directional sensitivity of a pitot tube allows, so that the measured pressures were too low.

In the following, only grid 1 is considered initially. For large distances from the grid ($x_1 = 69.2$ cm) the values of a , b , and c were measured for each measurement point, and the total pressure d was measured with the pitot tube. The t -values produced with this profile were all on the calibration curve which we plotted in the free jet, so that the static pressure here could be determined at each measurement point, as well as the velocity. Measurements were now made in steps of a few centimeters closer to the grid, so that the t -values became steadily larger. For constant x_1 these are distributed so that they are smallest for $\bar{y} = 0$ (jet center), and, conversely, greatest for $y = \pm \pi$ (center of the wake). They increase on approach to the grid.

Here

$$\bar{y} = \frac{2\pi y}{h}$$

and h is the grid separation, measured from bar axis to bar axis.

Now a velocity profile was selected which exhibits t -values extending above the measured calibration curve at measurement points lying in the vicinity of $\bar{y} = \pm \pi$. In order to satisfy continuity, the same average velocity U_0 must occur with this profile as with a profile with larger x_1 . As the velocity profiles for large x

/ 300

take on rather exact cosine shapes (7) one can approximately determine the position of the mean velocity by filling in the points where measurements are missing according to a cosine law. Now our three values a , b , and c are interpolated for these points, and the following value, from continuity:

$$(g - p_{st})/(a - b)$$

is plotted versus t in a new calibration curve. Here

$$g - p_{st} = \frac{\rho}{2} U_0^2$$

This curve is then improved in steps by complete calculation of individual velocity profiles and supplementary checking of the continuity

$$\int_{-\pi}^{+\pi} u \, d\gamma = \text{const.},$$

until it can finally be put in the form of Figure 6. For $t \leq 1.00$, other individual calibration points were obtained from measurements at a large distance from the grid.

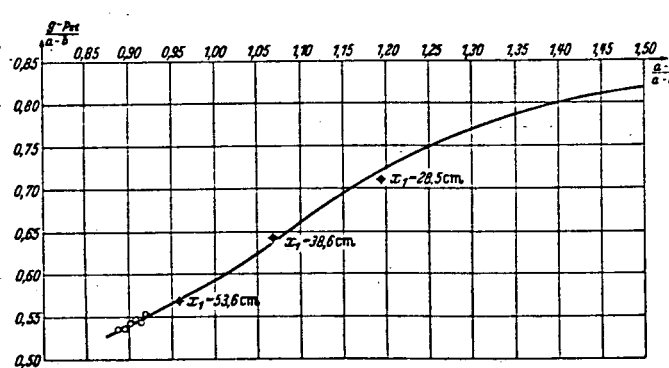


Figure 6. Calibration curve for calculation of the dynamic pressure.

(7) See Footnote 2, page 2.

The static pressure was determined similarly. From the momentum law it follows that

$$\frac{1}{2\pi} \int_{-\pi}^{+\pi} (\rho u^2 + p) d\bar{y} = \text{const } t,$$

if the small axial force σ_x is neglected (8). The momentum transport through the lines $\bar{y} = \pm \pi$ vanishes for reasons of symmetry. The value of the constant is determined from measurement for large distances from the grid. Then, for smaller and smaller x_1 the mean pressure p'_{st} is determined from the momentum law and the value of $(a - p'_{st})/(a - b)$ is plotted for the matching a , b , and c versus the corresponding t . The points obtained in this way are plotted as Φ in the calibration curve. The curve obtained in this manner was improved by complete calculation of individual pressure curves and repeated checking from the momentum law. Figure 4 shows the final form. As can be seen from the scattering of the calibration points, a small deviation from the curve obtained by calibration in the free jet is without any great importance, particularly because this also increases as t increases. From the four different designations of the calibration points, we can determine the a curve upon which we find ourselves.

/ 301

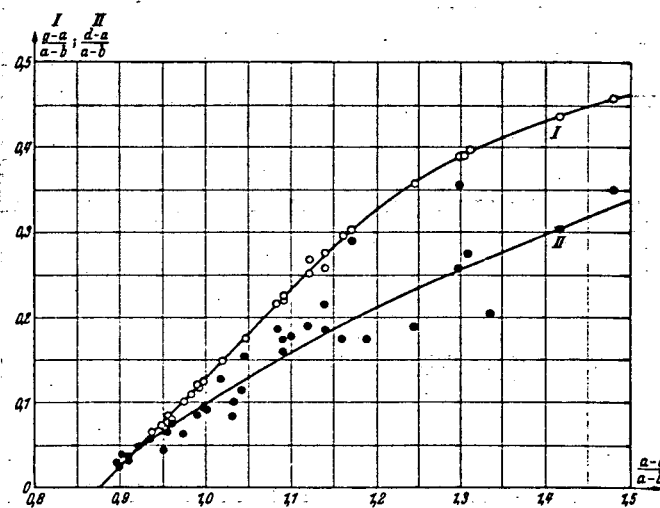


Figure 7. Dependence of $(g - a)/(a - b)$ and $(d - a)/(a - b)$ upon the measure of turbulence, t (obtained from experimental points with grid I.

(8) See Footnote 2, page 2.

Finally, by subtracting the ordinates of our two calibration curves, we obtain a relation between $(g - a)/(a - b)$ and our measure of turbulence, t , which provides us a determination of the true total pressure g (Figure 7). In order to show the deviation of the pressure indication d of the pitot tube from the true total pressure, $(d - a)/(a - b)$ is also plotted versus t (• in Figure 7). There is severe scattering here, to be sure, but it is no doubt related to the fact that with large t the flow direction usually diverges very strongly from parallelism with the long axis of the channel. Only our probe, through zero point determination, always remains adjusted in the flow direction, while the pitot tube remains unchanged.

3. The Grid Measurements

Using the measuring method developed above, measurements were made behind three grids. Their characteristic quantities h and λ can be determined from the following table:

	h (cm)	λ
G I	14.62	0.308
G II	10.20	0.462
G III	7.90	0.615

G II and GIII were produced from G I by adding one more grid bar for each, so that the ratio λ was increased correspondingly (Figure 8). All the grids were arranged so that no grid bar was directly adjacent to the channel wall, but rather so that a gap having a width equal to $2/3$ of the space between the nearest edges of the grid bars remained at the top and bottom. Experiments have shown that it is undesirable to have a grid bar immediately adjacent to the channel wall, because the dead space forming behind it extends too far into the flow as a perturbation. If one were to

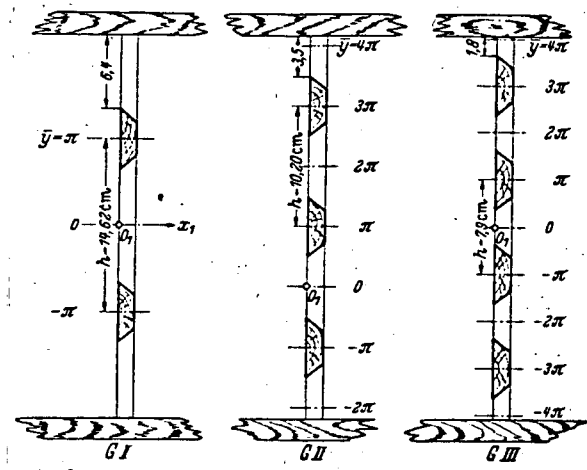


Figure 8. Schematic representation of the three grids.

decrease the gap width significantly, then the jet passing through would have insufficient energy to overcome the friction at the dead space of the adjacent bar, which is always greater than the wall friction.

/ 302

If we consider the velocity distribution behind Grid I, plotted versus \bar{y} for various values of x_1 (Figure 9), then we see that the maximum velocity is on the line $\bar{y} = 0$ for all x_1 . Here, therefore, we are dealing with the desired "stable" case for the application as a smoothing grid.

From Figure 10 we can determine the deviations of the measured total pressure from the true total pressure and from pressure a . We see that these become steadily smaller with increasing x_1 . For $x_1 = 69.2 \text{ cm}$ the measured and true total pressures are identical. At small x_1 the ambiguity of the pressures a , which we have already mentioned, appears. We see an example of this in Figure 10a. These measurements were made at a distance of $x_1 = 11 \text{ cm}$ from the grid.

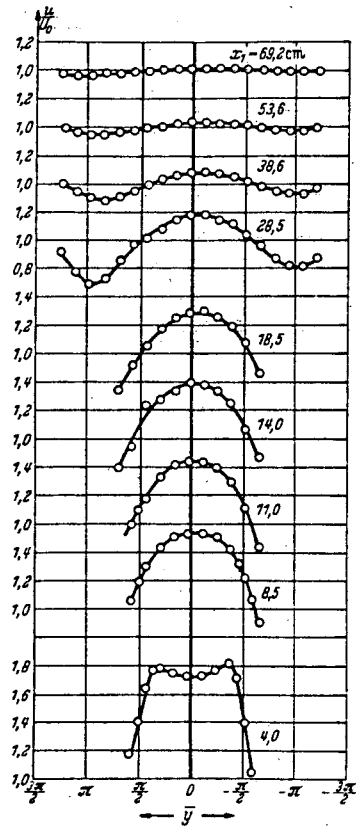


Figure 9. Velocity distribution behind Grid I.

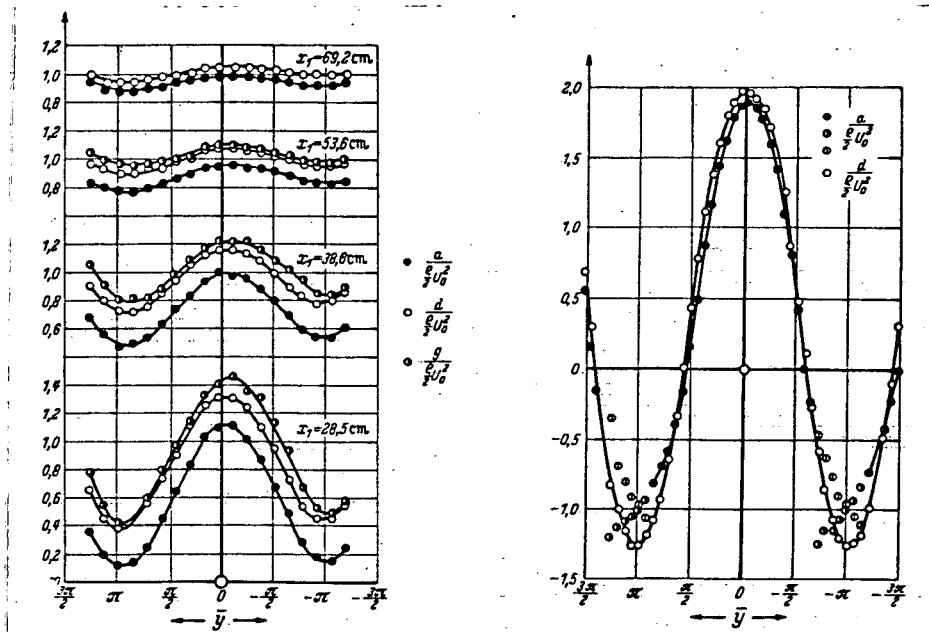


Figure 10. Dimensionless plot of d , d , and a behind Grid I.

Figure 10a. Curve of d and a versus \bar{y} for $x_1 = 11$ cm.

A dimensionless curve of pressure versus x_1/h was plotted for $\bar{y} = 0, \pi/2$, and π (Figure 11). The mean dynamic pressure was 6.12 kg/m^2 .

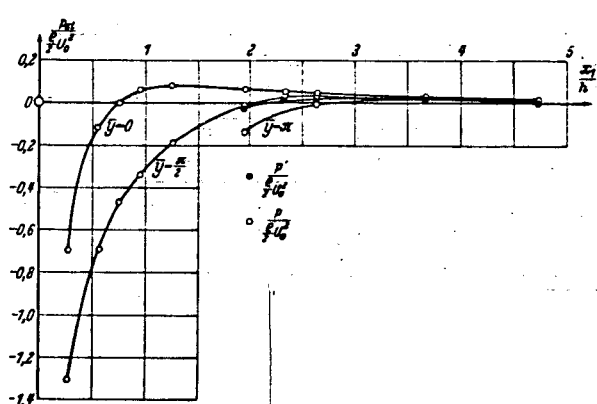


Figure 11. Pressure curve behind Grid I for $\bar{y} = 0, \frac{\pi}{2}, \pi$

The situation is different if λ is increased beyond the stability limit, as is the case for Grid II. We can at once see the instability in the velocity profiles (Figure 12a). Of the four jets passing the three grid bars, each pair unites, remaining parallel to the channel walls. At the center, then, i. e., for $\bar{y} = \pi$, a region with reverse flow is observed out to a distance of $x_1 = 14 \text{ cm}$ from the grid. To be sure, no measurements are plotted there, because at these points of low velocity the pressures a, b, and c often differ only by less than 1 mm alcohol, which does not provide sufficiently accurate readings with the instability of the entire flow.

With a small shift of the center grid bar (see also Figure 8) both the two outer jets remain at the channel walls, while the two central ones combine (Figure 12b). Here, again, as in the following figures, we must mention the gaps in the individual velocity profiles, which are based on the inaccuracy of the pressure readings mentioned above. To improve the clarity, the negative velocities are shaded in the figures.

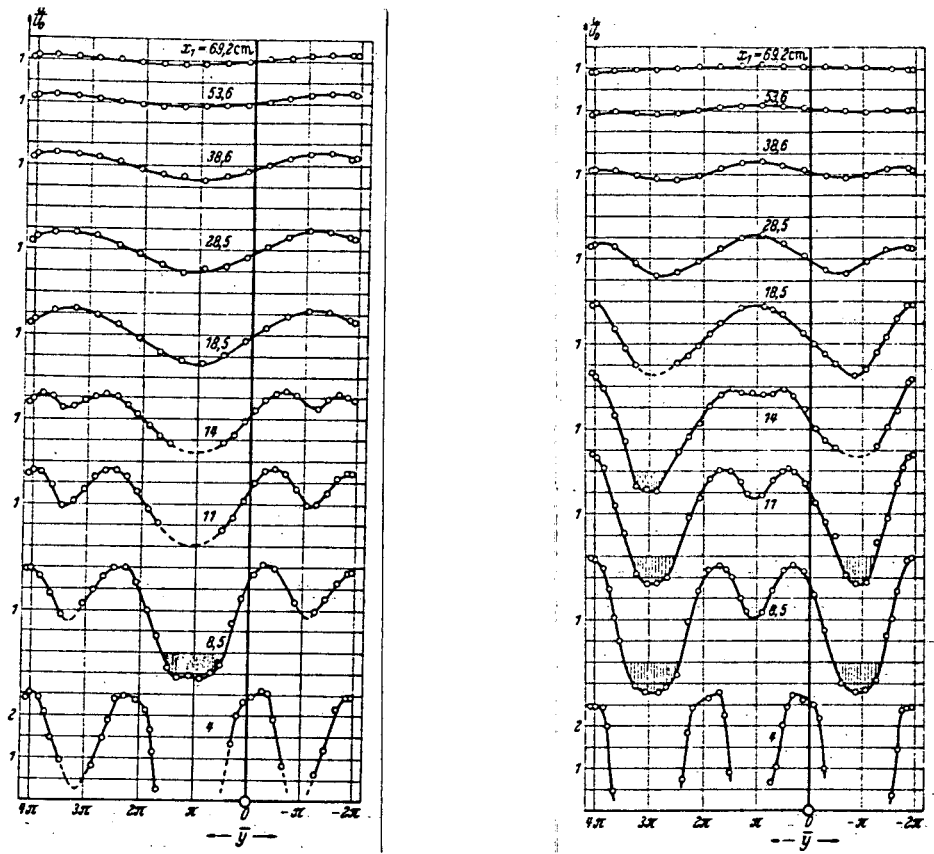


Figure 12 a and b. Velocity distribution behind Grid II.

/304

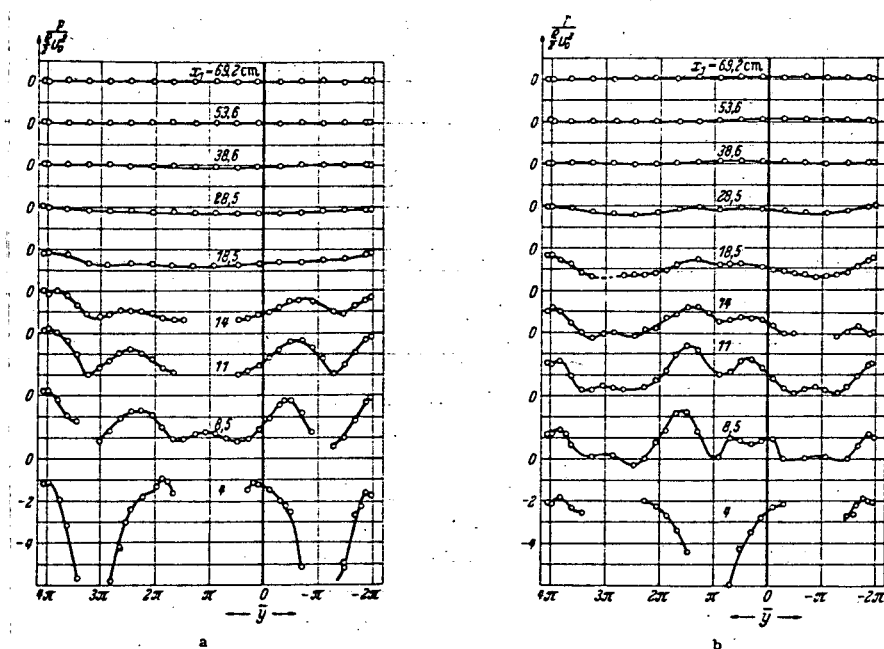


Figure 13 a and b. Curves of the static pressure for Grid II.

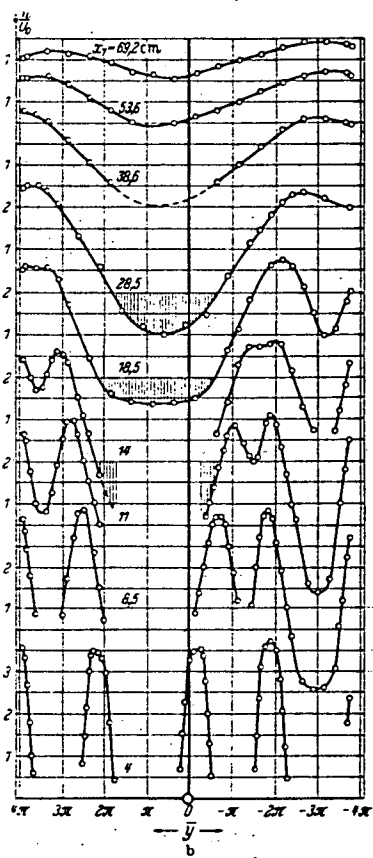
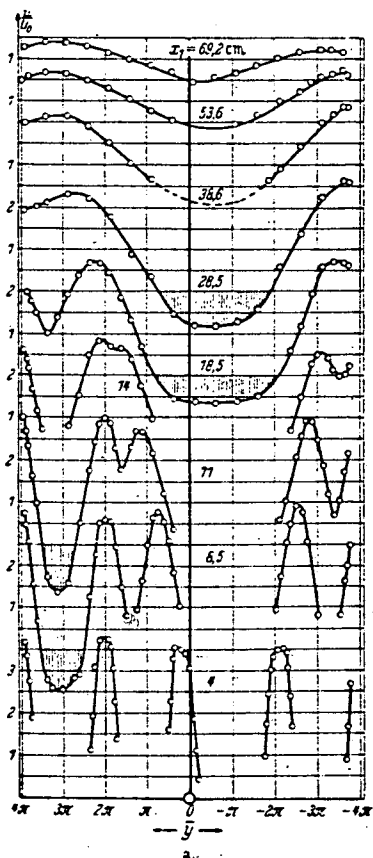


Figure 14 a and b. Velocity distribution behind Grid III.

The matching pressure curves can be seen in Figure 13a and Figure 13b.

With Grid III the second grid bar could be moved in the x_1 direction from below. It was possible to study the effect of small shifts in the x_1 direction on the velocity profile. All the velocities measured for $x_1 = 18.5$ cm are shown in Figure 15. This study has led to no new results. We see only that the central jet

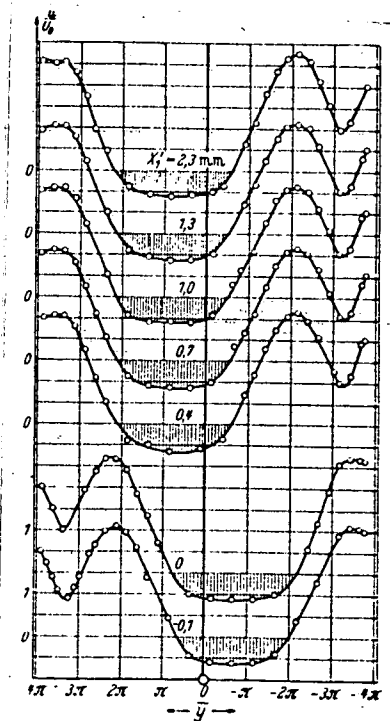


Figure 15. Velocity distribution for $x_1 = 18.5$ cm with shifts (x'_1) of the second grid bar from below.

combines either with the two upper jets (Figure 14a) or with the two lower ones (Figure 14b). The latter case occurs if the grid rod specified above is moved more than 0.4 mm in the x_1 direction. Here the dead space in the center extends particularly far in the flow.

Figure 16a and Figure 16b show the matching curves for the static pressure.

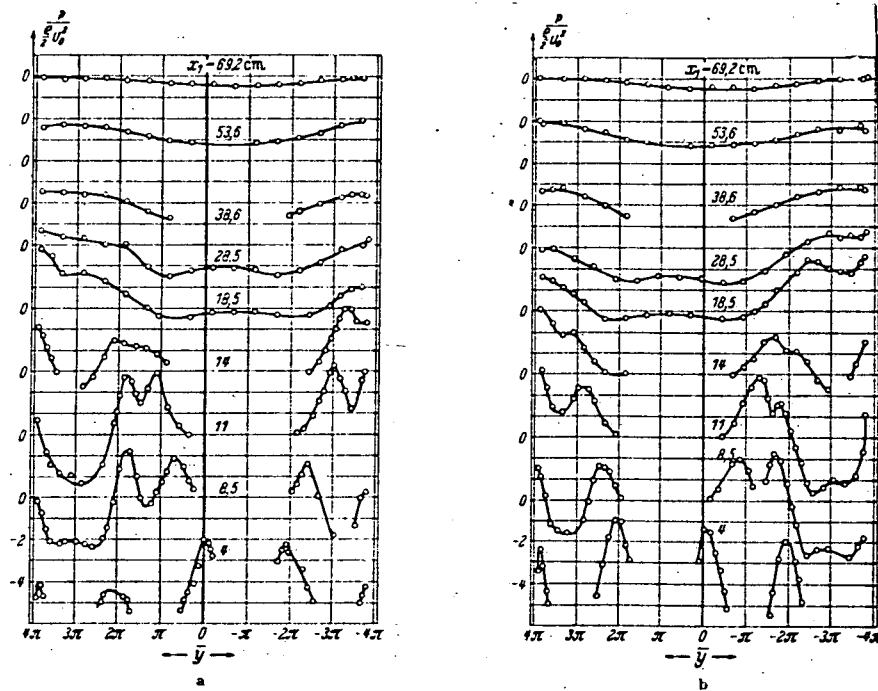


Figure 16 a and b. Curves for the static pressure with Grid III.

Mechanical inaccuracies in the grid structure are the cause for one or the other position of the jets being preferred; but if these inaccuracies are too small, then even stopping and restarting the motor can produce a different position of the jets. As mentioned previously, this phenomenon, which is undesirable for the measurement, was avoided by small intentional shifts of one grid bar.

The mean dynamic pressure was 6.10 kg/m^2 for Grid II and 5.26 kg/m^2 for Grid III.

II. Theoretical Part

1. The Hydrodynamic Statement

The instability we have observed for the jets passing through our grid occurs if the ratio λ , which we have defined on page 1, exceeds a value between 0.37 and 0.46. Now we shall attempt to confirm this instability analytically. For this purpose we make use of the method of small oscillations in which we superimpose upon a basic flow parallel to the x -axis with the flow function

$$\psi_1 = U_0 y + \frac{A(x)}{\alpha} \sin \alpha y \quad (1)$$

a perturbing flow with the flow function

$$\psi' = \frac{B(x)}{\beta} \sin \beta y \quad (2)$$

We presume the decay law for the amplitude $A(x)$ to be already known in the following. Now assume that

$$\beta < \alpha$$

that is, many jets of the basic flow impinge on one perturbing wave ⁽⁹⁾. Let the displacement experienced by the basic flow, ψ_1 , due to the perturbing flow, ψ' , be ξ_1, η_1 , and let ξ be neglected in relation to x as a first approximation. Then we can write

$$v' = \frac{D\eta}{dt} \approx U_0 \frac{\partial \eta}{\partial x} \quad (3)$$

for the velocity component v' of the perturbing flow, considered to be steady, if we neglect small terms in forming the material

(9) To be sure, in the numerical examples we have set $\beta = \frac{1}{2}\alpha$; i. e., two jets on one perturbing wave, so that not much more than a qualitative agreement by the calculation can be expected.

derivatives and average across the jets. On the other hand, it is also true for the velocity components of the perturbing flow that

$$u' = \frac{\partial \psi'}{\partial y}, \quad v' = -\frac{\partial \psi'}{\partial x}. \quad (4)$$

Correspondingly, according to (3),

$$\eta(x, y) = \int \frac{v'}{U_0} dx = -\frac{\psi'}{U_0} \quad (5)$$

(The arbitrary function of y , which properly must also be added to this, can be set equal to zero by appropriate definition of the points from which the displacement η is calculated).

It is also desirable to represent the total flow by a flow function. As the jets are directed to the side by the perturbing flow, u' , v' , according to (1), then we can write for this

$$\psi = U_0(y - \eta) + \frac{A(x)}{\alpha} \sin \alpha(y - \eta). \quad (6)$$

/ 307

Here, according to (5), the flow function for the perturbing flow is expressed by the term $-U_0\eta$. The velocities are determined from (6):

$$\begin{aligned} u &= \frac{\partial \psi}{\partial y} = \left(1 - \frac{\partial \eta}{\partial y}\right) [U_0 + A(x) \cos \alpha(y - \eta)], \\ v &= -\frac{\partial \psi}{\partial x} = -\frac{A'(x)}{\alpha} \sin \alpha(y - \eta) + A(x) \frac{\partial \eta}{\partial x} \cos \alpha(y - \eta) + U_0 \frac{\partial \eta}{\partial x}. \end{aligned} \quad (7)$$

By averaging across the jets we obtain

$$\bar{u} = U_0 \left(1 - \frac{\partial \eta}{\partial y}\right), \quad \bar{v} = U_0 \frac{\partial \eta}{\partial x}, \quad (8)$$

which agrees with Equations (3) to (5).

2. Approximate Solution of the Problem

As a strict solution of the problem formulated in the preceding cannot be carried out, the hydrodynamic differential equations were replaced by those obtained through averaging the velocities across the individual jets. The effect of turbulence is expressed by the apparent viscosity ϵ . Let us assume that this is a function of x alone, and, therefore, that it is independent of y . For the normal turbulence case, one can write, according to a statement by Prandtl (10):

$$\epsilon(x) = \rho l^2 \sqrt{\left(\frac{\partial u}{\partial y}\right)^2 + l^2 \left(\frac{\partial^2 u}{\partial y^2}\right)^2}. \quad (8)$$

If we insert into this

$$u = A(x) \cos \frac{2\pi y}{h} \quad \text{und} \quad l' = \frac{h}{2\pi}, \quad (d)$$

then with

$$\bar{l} = \frac{2\pi l'^2}{h} \quad (e)$$

obviously

$$\epsilon = \rho \bar{l} A(x). \quad (9)$$

According to experiments by Cordes (11), $l = 0.103 h$, giving $\bar{l} = 0.066 h$. (See the discussion on pages 22 - 24 for an expression for ϵ which more suitable for large x .)

Thus, the differential equations for the average motions become

$$\frac{\partial}{\partial x} (\bar{u}^2) + \frac{\partial}{\partial y} (\bar{u}v) + \frac{1}{\rho} \frac{\partial \bar{p}}{\partial x} = \frac{1}{\rho} \left[\frac{\partial}{\partial x} \left(2\epsilon \frac{\partial \bar{u}}{\partial x} \right) + \epsilon \left(\frac{\partial^2 \bar{u}}{\partial y^2} + \frac{\partial^2 \bar{v}}{\partial x \partial y} \right) \right], \quad (10)$$

$$\left[\frac{\partial}{\partial x} (\bar{u}v) + \frac{\partial}{\partial y} (\bar{v}^2) + \frac{1}{\rho} \frac{\partial \bar{p}}{\partial y} = \frac{1}{\rho} \left[\frac{\partial}{\partial x} \left(\epsilon \left(\frac{\partial \bar{u}}{\partial y} + \frac{\partial \bar{v}}{\partial x} \right) \right) + 2\epsilon \frac{\partial^2 \bar{v}}{\partial y^2} \right] \right]. \quad (11)$$

(11) See also Footnote 2, pg. 295.

The terms containing ϵ on the right side of Equations (10) and (11) appear because instead of the ordinarily used expression, $\epsilon \partial u / \partial y$ we have introduced the complete stress tensor $\epsilon(Ew + \eta \Gamma)$. As a result, η has the components u and v . Thus we obtained for the shear stress and the normal stresses the expressions

$$\left. \begin{aligned} \tau_{xy} &= \epsilon \left(\frac{\partial u}{\partial y} + \frac{\partial v}{\partial x} \right), \\ \sigma_x &= 2\epsilon \frac{\partial u}{\partial x}, \\ \sigma_y &= 2\epsilon \frac{\partial v}{\partial y}. \end{aligned} \right\} \quad (12)$$

Now, with our expressions for u and v from (7) we enter our Equations (10) and (11). In doing so, we note that $\eta(x, y)$ is considered to be a small value, and that as a first approximation we may neglect terms of higher order. In averaging across the region $|h = 2\pi/\alpha|$, which is assumed to be small, the quantities dependent on the perturbing flow (η) are considered constant. Likewise, we can write $\cos \alpha \eta \approx 1$ and $\sin \alpha \eta \approx \alpha \eta$, so that we can set

$$\left. \begin{aligned} \sin \alpha (y - \eta) &= \sin \alpha y - \alpha \eta \cos \alpha y, \\ \cos \alpha (y - \eta) &= \alpha \eta \sin \alpha y + \cos \alpha y \end{aligned} \right\}$$

All terms in the averages of (10) and (11) which contain a sine, cosine, or the product of both trigonometric functions as a factor are, therefore, replaced by their average value of zero. Only the terms with $\sin^2 \alpha y$ and $\cos^2 \alpha y$ make non-zero contributions. Considering these rules, we arrive after some computation at the two equations:

$$AA' - 2 \frac{\partial \eta}{\partial y} AA' + \frac{\partial^2 \eta}{\partial y^2} \frac{\epsilon U_0}{\rho} - \frac{\partial^2 \eta}{\partial x \partial y} \left(U_0^2 + \frac{A^2}{2} - \frac{2\epsilon' U_0}{\rho} \right) + \frac{\partial^2 \eta}{\partial x^2 \partial y} \frac{\epsilon U_0}{\rho} + \frac{1}{\rho} \frac{\partial p}{\partial x} = 0, \quad (13)$$

$$\frac{\partial \eta}{\partial x} AA' + \frac{\partial^2 \eta}{\partial x^2} \left(U_0^2 + \frac{A^2}{2} - \frac{\epsilon' U_0}{\rho} \right) - \frac{\partial^2 \eta}{\partial x^3} \frac{\epsilon U_0}{\rho} + \frac{\partial^2 \eta}{\partial y^2} \frac{\epsilon' U_0}{\rho} - \frac{\partial^2 \eta}{\partial x \partial y^2} \frac{\epsilon U_0}{\rho} + \frac{1}{\rho} \frac{\partial p}{\partial y} = 0. \quad (14)$$

(Strokes indicate differentiation with respect to x .)

In order to eliminate the pressure, we differentiate (13) with respect to y and (14) with respect to x and subtract the two equations. The result is a fourth-order partial differential equation for $\eta(x, y)$:

$$\left. \begin{aligned} \frac{\epsilon U_0}{\rho} \Delta \eta + \left(\frac{2\epsilon' U_0}{\rho} - U_0^2 - \frac{A^2}{2} \right) \frac{\partial}{\partial x} \Delta \eta - 2AA' \Delta \eta - \\ - \frac{\epsilon'' U_0}{\rho} \frac{\partial^2 \eta}{\partial y^2} + \frac{\epsilon'' U_0}{\rho} \frac{\partial^2 \eta}{\partial x^2} - (AA'' + A'^2) \frac{\partial \eta}{\partial x} = 0. \end{aligned} \right\} \quad (15)$$

Now if we return to the statement for η in (5), with (2) we obtain

$$\eta = -\frac{\psi'}{U_0} = -\frac{B(x)}{\beta U_0} \sin \beta y. \quad (16)$$

After an easy calculation we obtain, using (16) and through introduction into (15) of an ordinary fourth-order differential equation for the desired function $B(x)$:

$$\left. \begin{aligned} B'''' + B''' \left(\frac{2\epsilon'}{\epsilon} - \frac{\rho U_0}{\epsilon} - \frac{\rho A^2}{2\epsilon U_0} \right) + B'' \left(\frac{\epsilon''}{\epsilon} - \frac{2\rho AA'}{\epsilon U_0} - 2\beta^2 \right) - \\ - B' \left(\frac{2\epsilon' \beta^2}{\epsilon} - \frac{\rho U_0 \beta^2}{\epsilon} - \frac{\rho A^2 \beta^2}{2\epsilon U_0} + \frac{\rho AA''}{\epsilon U_0} + \frac{\rho A'^2}{\epsilon U_0} \right) + B \left(\beta^4 + \frac{2\rho AA' \beta^2}{\epsilon U_0} + \frac{\epsilon'' \beta^2}{\epsilon} \right) = 0. \end{aligned} \right\} \quad (17)$$

Now, before proceeding with our calculation, we must make some introductory comments on the decay law of $A(x)$.

Gran Olsson (12) and Cordes (13), according to the ordinary turbulence statement of (8), have found that $A(x)$ decays as $1/x$. They have also confirmed this by measurements. But from measurements by Dryden and others, it appears that for large values of x/h (h = grid division), $A(x)$ decays in proportion to $(x/h)^{-n}$, with $n > 1$. If the grid bars become wider and, thus, the turbulence produced by the grid becomes stronger, this is the case even for small x/h , as shown by the present work. From measurements by Dryden, Prandtl has derived an n in the vicinity of 4.5 for this

(12) R. Gran Olsson, Z. Angew. Math. Mech. 16(1936), page 257.

(13) See footnote 2, page 2.

investigated case. According to the current concept, the state of turbulence behind the grid more and more approaches the so-called "isotropic" turbulence, falling off with time, with increasing distance from the grid. Here the old statement for the apparent viscosity η in (8) is no longer valid, because du/dy vanishes there. Therefore, Prandtl ⁽¹⁴⁾ developed an expanded statement, according to which finite values of the turbulent agitation remain even where du/dy is already zero, as detailed experimental observations require. This statement contains the comment that the transverse gradient of the mean velocity u which was present at a certain time t' contributes to the instantaneous state of turbulence at a later time t . With a shear stress term matched to this concept, the larger values of n required by observation could also be obtained theoretically.

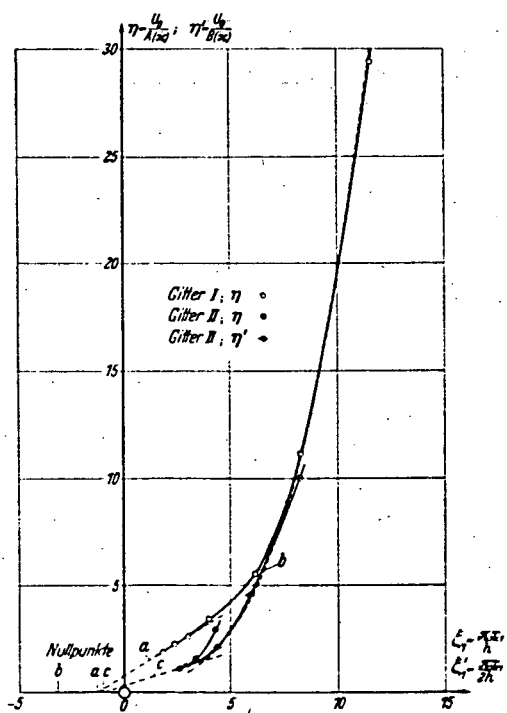


Figure 17. Dependence of $\eta = \frac{\tau}{u_{\max} - u_s}$ on Re_1 (obtained from the velocity profiles of Figures 9 and 12b). The dashed lines a, b and c represent the formulas (20), (21), and (20a).

(14) Lecture at the International Congress on Mechanics, Cambridge, USA, 1938.

Using this statement, one obtains, instead of (9), the following expression for ε :

$$\varepsilon = \varrho \frac{n}{\alpha^2} \frac{U_0}{x} \quad (18)$$

(with $\alpha = 2\pi/h$, where x is not the distance from the grid, but from an initial point situated upstream from the grid). The exponent of n can be determined practically by plotting the value of the ratio $\eta = U_0/(u_{\max} - U_0) = U_0/A(x)$ versus the distance x_1 of the measurement cross section from the plane of the grid, or better, the ratio x_1/h .

As the theory developed above is to be applied to the special case occurring in the experiments, where the two jets combine beyond a distance h and so form new jets from the distance $2h$, here we must set $\beta = \frac{1}{2}\alpha$. For further calculation it proves expedient to introduce a dimensionless variable $\xi_1 = x_1\beta$ which, with $\beta = \frac{1}{2}\alpha$ and $\alpha = 2\pi/h$, gives

$$\xi_1 = \frac{\pi x_1}{h} \quad (19)$$

Figure 17 shows a plot of η in dependence on ξ_1 , based on the measurements for Grid I given in Figure 9. The first part of the curve can be reproduced by a straight line with the equation

/310

$$\eta = \frac{1,879}{h} (x_1 + 0,407 h) = 0,598 (\xi_1 + 1,278) \quad (20)$$

In the following, we set $\xi_1 + 1,278 = \xi$; therefore, $\eta = 0,598\xi$. This line is marked a in Figure 17.

For $\xi_1 > 7$, $A(x)$ decreases approximately with $(x_1 + e')^{-4}$, with $e' \approx h$, giving

$$\eta = 0,00064 (\xi_1 + 3,14)^4 \quad (21)$$

For simplicity, we write the formula

$$\xi_1 + 3,14 = \bar{\xi}$$

in the following. In Figure 17, Formula (21) is marked as b.

For Grid II there is, from the first measuring cross sections, a strong amplitude of the oscillation $B(x)$, which is superimposed on the original amplitude $A(x)$, but which has twice the wavelength. The course of the amplitude $A(x)$ is determined here in such a way that the velocity profile of Figure 12b is analyzed into its A component and B component. The curve for the two components is also shown in Figure 17. Corresponding to the doubled wavelength of B, $\xi_1 = \pi x_1 / 2h$ is plotted instead of ξ_1 for these values. As it appears, the A curve is strongly curved from the beginning due to the increased turbulence related to the B amplitude. In order to apply our formula, at the first A point, in place of (20) a linear function is assumed, which runs approximately tangential to this curve. The formula used for this is

$$\eta = 0,31(\xi_1 + 1,0) \quad (20a)$$

(the approximations which led to the selected zero point shift can be passed over here). Formula (21) can be used with sufficient accuracy for the value of η , if ξ_1 in it is replaced by ξ_1 .

Now we return to Equation (17) and make it dimensionless by defining the following quantities:

$$\left. \begin{aligned} B(x) &= U_0 D(\xi), & \xi &= \xi_1 + e\beta, \\ \overline{I}\beta &= \gamma, \\ \frac{\xi A(x)}{U_0} &= \delta. \end{aligned} \right\} \quad (22)$$

With these dimensionless quantities, (17) transforms into

$$\left. \begin{aligned} D''''(\xi) - D'''(\xi) \left(\frac{4\gamma + \delta}{2\gamma\xi} + \frac{\xi}{\gamma\delta} \right) + D''(\xi) \left[\frac{2(\gamma + \delta)}{\gamma\xi^2} - 2 \right] + \\ + D'(\xi) \left(\frac{4\gamma + \delta}{2\gamma\xi} + \frac{\xi}{\gamma\delta} - \frac{3\delta}{\gamma\xi^3} \right) + D(\xi) \left[1 + \frac{2(\gamma - \delta)}{\gamma\xi^2} \right] = 0. \end{aligned} \right\} \quad (23)$$

Here we must note that this differential equation is valid only in the range within which $A(x)$ is proportional to x^{-1} . Direct solution is possible only through the series expression

$$D(\xi) = \sum_{r=0}^{\infty} a_r \xi^{\sigma+r} \quad (24)$$

Unfortunately the convergence region of the series arising in the solution ends in the vicinity of the grid plane, just at the point beyond which we begin to be interested in the course of $D(\xi)$. An approximate discussion of the properties of the solution appears on page 29.

/ 311

In order to see how the solutions behave for larger values of ξ where A is proportional to ξ^{-n} , we introduce into Equation (23) instead of γ

$$\bar{\gamma} = \frac{n\beta^2}{\alpha^2} \quad \text{und} \quad \bar{\delta} = \frac{\xi^{2n} A^2}{U_0^2} \quad (25)$$

Here

$$\bar{\xi} = \xi_1 + \frac{e' \pi}{h} \quad [e' \text{ aus (21)}]. \quad (26)$$

The extended statement for $\bar{\xi}$ is taken from (18) so that, after introducing the specified quantities, we can now obtain from (17):

$$\left. \begin{aligned} D''''(\bar{\xi}) - D'''(\bar{\xi}) \left(\frac{\bar{\xi}}{\bar{\gamma}} + \frac{2}{\bar{\xi}} + \frac{\bar{\delta}}{2\bar{\gamma}\bar{\xi}^{2n-1}} \right) - D''(\bar{\xi}) \left(2 - \frac{2}{\bar{\xi}^2} - \frac{2n\bar{\delta}}{\bar{\gamma}\bar{\xi}^{2n}} \right) + \\ + D'(\bar{\xi}) \left[\frac{\bar{\xi}}{\bar{\gamma}} + \frac{2}{\bar{\xi}} + \frac{\bar{\delta}}{2\bar{\gamma}\bar{\xi}^{2n-1}} - \frac{n(2n+1)\bar{\delta}}{\bar{\gamma}\bar{\xi}^{2n+1}} \right] + D(\bar{\xi}) \left(1 + \frac{2}{\bar{\xi}^2} - \frac{2n\bar{\delta}}{\bar{\gamma}\bar{\xi}^{2n}} \right) = 0. \end{aligned} \right\} \quad (27)$$

As can be seen from the pattern of the coefficients, solution of this differential equation by means of an asymptotic series of the form

$$D(\bar{\xi}) = \sum_{r=0}^{\infty} b_r \left(\frac{1}{\bar{\xi}} \right)^{\sigma+r}$$

is not possible. By neglecting the terms in the individual coefficients which become small for large $\bar{\xi}$ it was possible to find two

particular integrals of the differential equation simplified in this way:

$$D_1(\xi) = e^{\xi} \quad \text{und} \quad D_2(\xi) = e^{-\xi}$$

From the second-order differential equation obtained in this way, the two missing solutions can then be developed after further reasonable approximations.

But in order to link up with the solutions obtained from differential equation (23), we must not undertake the approximations just mentioned, because the neglected terms are not small at all in this range. We can see this immediately if we consider the values for γ and $\bar{\gamma}$ from the table below.

So as to be able first to study the behavior of our solutions by means of a simpler example, we write, temporarily,

$$\varepsilon = \rho k \frac{U_0}{\beta} = \text{const.}$$

Then, instead of (23), we obtain

$$D''''(\xi) - D'''(\xi) \frac{1}{k} - 2D''(\xi) + D'(\xi) \frac{1}{k} + D(\xi) = 0. \quad (28)$$

With

$$D(\xi) = e^{\sigma \xi}$$

we obtain, for the roots σ of the principal equation

$$\left. \begin{aligned} \sigma_1 &= \frac{1}{2k} + \sqrt{\frac{1}{4k^2} + 1} \approx \frac{1}{k} + k + \dots, & \sigma_2 &= -1, \\ \sigma_3 &= +1, & \sigma_4 &= \frac{1}{2k} - \sqrt{\frac{1}{4k^2} + 1} \approx -k - \dots. \end{aligned} \right\} \quad (29)$$

As k is supposed to be much less than unity, σ_1 becomes large and positive, and σ_4 small and negative, while σ_2 and σ_3 are of normal magnitude.

It is well known that the potential flows, which one knows from the frictionless liquid, belong to the solutions of the Navier-Stokes differential equations. The solutions built up with σ_2 and σ_3 in our case are of that type. The term $D_2(\xi)$ decays with increasing ξ like a disturbance produced by an upstream barrier which is periodic with y , while $D_3(\xi)$ is explained by the diversion of the basic flow before a downstream barrier which is periodic with y . With σ_4 , we obtain the solution being considered for our flow with lower apparent viscosity. As we can see from the binomial expansion of σ_4 , it decays slowly with ξ . The term $D_1(\xi)$ increases strongly ahead of the downstream barrier. Thus, it is suited to represent the asymptotic behavior of the velocity changes occurring through a turbulent boundary layer before a barrier as it approaches the barrier.

Now, in order to determine more accurately the properties of the solution of (23), as the strict solution is not attainable, the following expedient was taken: We investigated the approximation obtained if the whole region is dissected into a number of segments, so that the coefficients of (23) are inserted for each segment (from ξ_1 to ξ_2) with the constant value which they have in the center of the segment.

First, the following table will explain the numbers $[\gamma, \delta, \bar{\gamma}, \bar{\delta}]$ and n obtained from the experiment:

	Grid I	Grid II	
γ	0,210	0,210	
δ	1,671	3,226	
$\bar{\gamma}$	1,000	—	
$\bar{\delta}$	$2,441 \cdot 10^6$	—	
"	4,0	—	(30)

Now, using the values of γ and δ from (30), the coefficients of the differential equation (23) are calculated for three definite values of ξ , so that we obtain a differential equation with constant coefficients for each $\xi_i (i=a, b, c)$, the solutions of which also satisfy (23) in the near vicinity of the ξ concerned. The four resulting constants are left undefined, as a quantitative comparison with experiment cannot be performed. Now there appear the following differential equations for Grid I:

$$\left. \begin{array}{l} \text{for } \xi_a = 2,132: D''''(\xi) - 8,879D'''(\xi) + 1,949D''(\xi) + 6,412D'(\xi) - 2,073D(\xi) = 0, \\ \text{for } \xi_b = 3,202: D''''(\xi) - 10,900D'''(\xi) - 0,256D''(\xi) + 10,178D'(\xi) - 0,360D(\xi) = 0, \\ \text{for } \xi_c = 4,280: D''''(\xi) - 13,635D'''(\xi) - 1,020D''(\xi) + 13,330D'(\xi) + 0,238D(\xi) = 0. \end{array} \right\} \quad (31)$$

The corresponding differential equations for Grid II are:

$$\left. \begin{array}{l} \text{for } \xi_a = 1,854: D''''(\xi) - 7,959D'''(\xi) + 7,520D''(\xi) + 0,727D'(\xi) - 7,356D(\xi) = 0, \\ \text{for } \xi_b = 2,924: D''''(\xi) - 7,627D'''(\xi) + 1,827D''(\xi) + 5,784D'(\xi) - 2,360D(\xi) = 0, \\ \text{for } \xi_c = 4,002: D''''(\xi) - 8,326D'''(\xi) + 0,043D''(\xi) + 7,607D'(\xi) - 0,793D(\xi) = 0. \end{array} \right\} \quad (32)$$

In the same way, for Grid I, we derive three differential equations from (27):

$$\left. \begin{array}{l} \text{for } \xi_a = 11,14: D''''(\xi) - 11,377D'''(\xi) - 1,902D''(\xi) + 11,344D'(\xi) + 0,934D(\xi) = 0, \\ \text{for } \xi_b = 12,64: D''''(\xi) - 12,822D'''(\xi) - 1,957D''(\xi) + 12,811D'(\xi) + 0,983D(\xi) = 0, \\ \text{for } \xi_c = 14,14: D''''(\xi) - 14,292D'''(\xi) - 1,978D''(\xi) + 14,288D'(\xi) + 0,998D(\xi) = 0. \end{array} \right\} \quad (33)$$

/ 313

All the equations are solved with the statement

$$D(\xi) = Ce^{\sigma\xi}$$

or Equations (33) with

$$D(\xi) = Ce^{\sigma\xi}$$

The principal equations are solved for the roots σ_1 to σ_4 by Graeff's method. Their values are in the following table, which also includes the values of σ_1 to σ_4 for comparison with those from (28), as the former transform into the latter.

	σ_1	σ_2	σ_3	σ_4	
<u>Grid I</u>					(34a)
ξ_a	+ 8,558	-0,853	+ 0,827	+ 0,347	}
ξ_b	+ 10,837	-0,955	+ 0,982	+ 0,035	
ξ_c	+ 13,628	-0,971	+ 0,996	-0,018	
ξ_d	+ 11,456	-0,997	+ 0,9995	-0,0815	
ξ_e	+ 12,896	-0,9977	+ 0,9997	-0,076	
ξ_f	+ 14,360	-0,9979	+ 0,9999	-0,070	
<u>Grid II</u>					(34b)
ξ_a	+ 6,875	-0,750	$0,917 \pm 0,768i$		}
ξ_b	+ 7,272	-0,893	+ 0,784	+ 0,464	
ξ_c	+ 8,211	-0,951	+ 0,960	+ 0,106	

According to the considerations connected with Equation (29), the sign of the root σ_4 (or its real portion) must be considered decisive for stability or instability. Our calculations, from which not much more than a qualitative agreement with observations could be expected according to the comment in the footnote on page 19, accordingly show a moderate instability for the positions near the grid even for Grid I, but stability in the later course. Comparison with Grid II shows a distinct increase of the instability with Grid II. Recalculation of the state of Grid II after the transition to the doubled perturbing wavelength may be unnecessary, as numerical values of η are obtained for the turbulent exchange on replacement of ξ_1 by η according to Figure 17. They differ only slightly from those of Grid I according to (21). After the alteration, therefore, one would calculate for the state of Grid II flow a stability corresponding to that given for the positions ξ_a to ξ_f for Grid I.

As for instability on a short segment of the path, with subsequent stability, it should be noted that very small original perturbations can grow to dangerous size only on a long path. The overturning of the flow is, therefore, quite significantly supported by any sort of unevenness in the structure of the grid. When the experiments were being carried out, it actually appeared that Grid III (see Figure 8), for which λ has the greatest value of the grids studied, is the most sensitive to mechanical inaccuracies in the grid structure. When using a smoothing grid, then, it is desirable to design it so that the grid density λ does not exceed the value specified on page 2.

Summary

In order to explain the irregularities occurring in the flow behind smoothing grids, the flow was investigated behind three grids with different apertures. In order to obtain useful velocity measurements in this particularly severely turbulent flow, a probe was developed which could be calibrated in a free jet mixing zone. In order to measure the static pressure in a flow for which the turbulence is considerably stronger than that in a free jet mixing zone, calibration curves were derived to determine the static pressure, the total pressure, and the dynamic pressure in their dependence on a turbulence measure which the probe also provides. For each measurement point, three pressure readings are needed at different angles of rotation for the probe.

/ 314

For the grids studied it was found that the instability observed occurs more easily the more closely together the grid rods are built, with their widths remaining the same.

This phenomenon was followed up theoretically by application of the hydrodynamic equations of motion produced by averaging the velocities across the individual jets. The result confirmed the instability observed with Grid II and showed that even the flow from Grid I probably has an unstable region, which would have appeared

with greater displacement of a grid bar.

The experiment was performed at the Kaiser Wilhelm Institute for Flow Research at Göttingen.

Translated for National Aeronautics and Space Administration under contract No. NASw 2483, by SCITRAN, P. O. Box 5456, Santa Barbara, California, 93108